Machine learning techniques to construct detailed phase diagrams for skyrmion systems

F. A. Gómez Albarracín [*] and H. D. Rosales

Instituto de Física de Líquidos y Sistemas Biológicos (IFLYSIB), UNLP-CONICET, Facultad de Ciencias Exactas, La Plata, Argentina;
Departamento de Física, Facultad de Ciencias Exactas, Universidad Nacional de La Plata, La Plata, Argentina;
and Departamento de Ciencias Básicas, Facultad de Ingeniería, Universidad Nacional de La Plata, La Plata, Argentina

Recently, there has been an increased interest in the application of machine learning (ML) techniques to a variety of problems in condensed-matter physics. In this regard, of particular significance is the characterization of simple and complex phases of matter. Here, we use a ML approach to construct the full phase diagram of a well-known spin model combining ferromagnetic exchange and Dzyaloshinskii-Moriya (DM) interactions where topological phases emerge. At low temperatures, the system is tuned from a spiral phase to a skyrmion crystal by a magnetic field. However, thermal fluctuations induce two types of intermediate phases, bimerons and skyrmion gas, which are not as easily determined as spirals or skyrmion crystals. We resort to large-scale Monte Carlo simulations to obtain low-temperature spin configurations and train a convolutional neural network (CNN), taking only snapshots at specific values of the DM couplings, to classify between the different phases, focusing on the intermediate and intricate topological textures. We then apply the CNN to higher-temperature configurations and to other DM values to construct a detailed magnetic-field–temperature phase diagram, achieving outstanding results. We discuss the importance of including the disordered paramagnetic phases in order to get the phase boundaries, and, finally, we compare our approach with other ML algorithms.

I. INTRODUCTION

In the last five years, machine learning (ML) techniques have provided a new perspective on the study of a great variety of physical phenomena in condensed-matter physics, from representation of quantum states [1] to discovering phase transitions [2–4] and identifying conventional phases of matter [5]. The ability of ML to identify and classify huge data sets, including images, provides a powerful tool to analyze the state space of condensed-matter systems.

These approaches have been successfully applied to a variety of complex topological spin systems and models. For example, autoencoders have been used to extract models from neutron-scattering data in spin ice systems [6,7]. Support vector machines with a tensorial kernel have been used to explore tensor order parameters and hidden order in nontrivial frustrated models such as the XXZ model on the pyrochlore lattice [8], the classical kagome antiferromagnet [9], and Kitaev models and materials [10–12].

Among exotic phases, magnetic skyrmions are undoubtedly at the heart of a large body of work [13–15]. Skyrmions are swirling magnetic textures characterized by a topological invariant, the topological charge $Q = \frac{1}{4\pi} \int d^2 r \vec{S} \cdot (\partial_x \vec{S} \times \partial_y \vec{S})$ (where $\vec{S}$ is the unit vector of the local magnetization), which provides them with great stability against perturbations. Therefore, magnetic skyrmions have been intensively studied due to their potential in future magnetic data storage and spintronics applications. In fact, neural networks have been implemented in the last years to distinguish skyrmion phases. On one hand, a few years ago, it was shown that a single layer neural network can successfully classify standard configurations: spiral, ferromagnetic and skyrmion crystal [16], and a similar classification task was achieved with convolutional neural networks (CNNs) to construct low-temperature phase diagrams for models including anisotropy terms [17]. Recurrent neural networks were used to classify skyrmion dynamic processes [18]. On the other hand, CNNs were used to predict features such as chirality in these type of systems [19], even in confined geometries [20], and to extract information on the interactions from data images [21]. Moreover, taking input data from videos, these type of techniques were used to classify the dynamical skyrmion phases and to predict phase boundaries [22]. Most studies in this field have only focused on the characterization of typical configurations and not so much attention has been paid to the intermediate and less conventional phases emerging from thermal fluctuations.

In this regard, the aim of this investigation is to explore the capacity of machine learning algorithms to identify and classify all the magnetic phases in skyrmion systems. Our main goal is to apply these techniques to construct a complete magnetic-field–temperature (B-T) phase diagram for a well-known model where a skyrmion crystal is stabilized at low temperatures, the ferromagnetic square lattice with Dzyaloshinskii-Moriya (DM) interactions under an external magnetic field. Magnetic configurations for this study were collected using large-scale Monte Carlo simulations. Then, we resort to a convolutional neural network (CNN) to classify the lowest temperature phases, that include bimeron and skyrmion gas labels. The term "bimeron" here is used to refer to

_____
[*]albarrac@fisica.unlp.edu.ar, she/her/hers

elongated skyrmions or broken spirals [23–25] and to differentiate from the use of the term which refers to two merons [26].

As a first step, we train and validate the network for three specific values of the DM interaction. We then apply the trained model to other DM values and to higher temperature configurations, and build the complete B-T phase diagram, which we compare with results from simulations, finding remarkable agreement. In particular, our CNN-based approach shows that all types of topological phases considered could be distinguished and classified. Given that CNNs are techniques ideal for treating image data, this opens the door to use a similar approach for analysis of the experimental images obtained with spin-polarized scanning tunneling microscopy techniques, where these type of intermediate phases are usually found [27–30].

The paper is organized in the following way: In Sec. II we describe the model, discuss the emergent topological phases, and show the particular features of the bimeron and skyrmion gas configurations. The ML approach and analysis are described in Sec. III, where we also explore other simpler ML methods. Conclusions and future perspectives are presented in Sec. V.

II. SKYRMION MODEL

Skyrmions have been at the heart of a large body of work since the indirect experimental observation of skyrmion crystals through neutron diffraction in MnSi [31] and direct observation in thin films [27]. Research has also expanded to other topological textures [14,15], such as antiferromagnetic skyrmions [32–35], magnetic bubbles, merons and antimerons [36]. Here, we focus on a well-known skyrmion model, which was proposed to compare with one of the first bidimensional experimental phase diagrams [27], and has also been used to explore machine learning techniques for skyrmion phases [16,19]. We take the ferromagnetic exchange model with in-plane Dzyaloshinskii-Moriya interactions (DM) under a magnetic field for classical Heisenberg spins in the square lattice, given by

$$\mathcal{H} = -J \sum_{\langle i,j \rangle} \vec{S}_i \cdot \vec{S}_j + \sum_{\langle i,j \rangle} \vec{D} \cdot (\vec{S}_i \times \vec{S}_j) - \vec{B} \sum_i \vec{S}_i, \quad (1)$$

where $\vec{S}_i$ are Heisenberg spins at site i with fixed norm 1, J is the ferromagnetic exchange coupling, $\vec{D}$ is the in-plane DM interaction along the bonds of the square lattice (see inset in Fig. 1), and $\vec{B} = B\check{z}$ is the external magnetic field, perpendicular to the lattice plane. We take $J = 1$ throughout the rest of this work.

We briefly review here the well-known behavior of this model with magnetic field and temperature to motivate our study. We present in Fig. 1 the low-temperature phase diagram ($T \ll J$) as a function of the magnetic field B and the DM strength D. Regarding the magnetization process, the magnetic field takes the system from a spiral phase (Sp) induced at zero field for a small DM interaction [37] to a skyrmion crystal (SkX), and then to a ferromagnetic (Fm) state at higher B. There are two types of intermediate phases, which we will discuss further below: what we refer to here
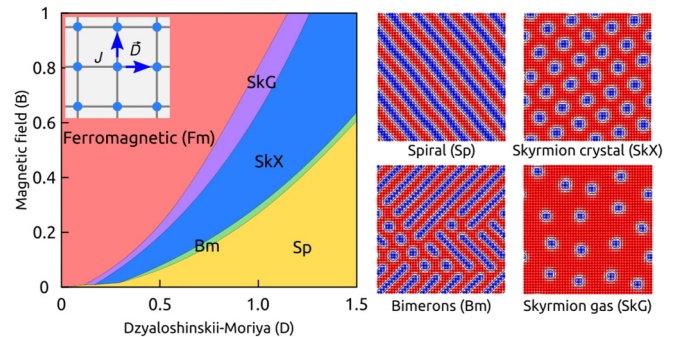

FIG. 1. (left) Low-temperature phase diagram for the ferromagnetic model in a square lattice with DM interactions under a magnetic field B. In the inset, (blue) arrows indicate the direction of the DM vectors, along the bonds of the square lattice. (right) Typical real-space configurations for the four different nonpolarized phases: spiral (Sp), bimeron (Bm), skyrmion crystal (SkX), skyrmion gas (SkG).

as a "bimeron" phase (Bm), which consists of a mixture of "broken spirals" or "elongated skyrmions" and skyrmions, and a second "skyrmion gas" phase (SkG), where the skyrmions no longer form a crystal and are distributed in a ferromagnetic background. These intermediate phases are enhanced by temperature and should disappear in the zero-temperature limit [23]. A detailed phase diagram for a similar system at larger system sizes may be found in Ref. [38]. We show typical real-space configurations for different phases on the right in Fig. 1.

The spiral skyrmion crystal and ferromagnetic phases can easily be distinguished by resorting to variables such as the scalar chirality χ and the structure factor $S_{\mathbf{q}}$. Throughout all this work, $S_{\mathbf{q}}$ refers to the structure factor calculated with the components of the spins perpendicular to the external magnetic field, $S_{\mathbf{q}} = \frac{1}{N} \langle | \sum_i S_i^x \, e^{i\mathbf{q} \cdot \mathbf{r}_i} |^2 + | \sum_i S_i^y \, e^{i\mathbf{q} \cdot \mathbf{r}_i} |^2 \rangle$, where N is the total number of spins. The scalar chirality, defined as $\chi = \sum_{i,j,k} \vec{S}_i \cdot (\vec{S}_j \times \vec{S}_k)$, is quantity in a lattice that is related to the calculation of the topological charge Q, which is $Q = -1$ for each skyrmion. Therefore, in the SkX phase, χ is nonzero and relates to the number of skyrmions, whereas the spiral and the ferromagnetic phase are not chiral, with $Q = 0$. As for $S_{\mathbf{q}}$, a SkX is characterized with six Bragg peaks in reciprocal space, where the three inequivalent $\mathbf{q}^*$ vectors satisfy $\sum_i \mathbf{q}_i = 0$ (triple-q phase). In a spiral phase, for this model, there would be two incommensurate Bragg peaks (single q). However, things are not so simple if we wish to take into account the intermediate phases. On one hand, the system does not present a clear transition between phases with temperature. On the other hand, especially at higher temperatures, these configurations do not have a characteristic structure factor. We illustrate this showing the results of Monte Carlo simulations for $D = 1$ in Figs. 2 ($B = 0.2$) and 3 ($B = 0.9$). In both cases, we plot the resulting specific heat and chirality as a function of temperature and show three different snapshots and their respective S_q at different temperatures. In Fig. 2, at $B = 0.2$, we see that, at low temperature, the system is in a Sp phase, with the typical single-q S_q. At higher T, there is nonzero chirality and the snapshots show a Bm phase, which goes from single-q to a less defined S_q. A similar behavior is seen at higher fields ($B = 0.9$) in Fig. 3, but comparing here
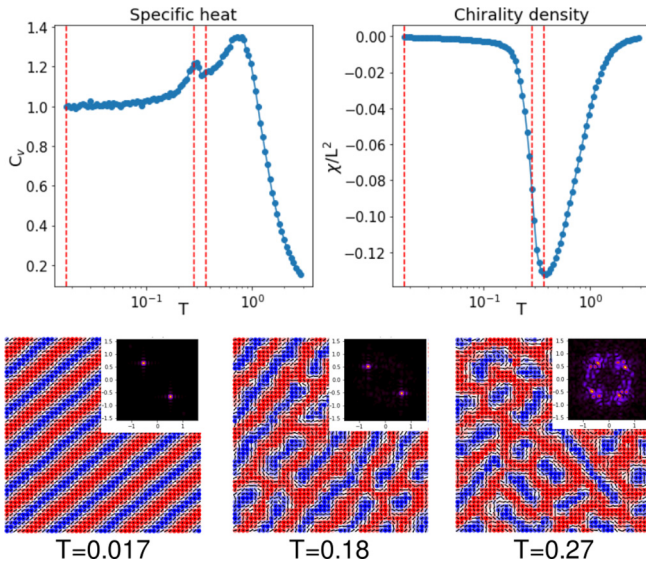
FIG. 2. Monte Carlo simulations for $D = 1$, $B = 0.2$. (top) Specific heat, magnetization, and chirality as functions of temperature. (bottom): Three snapshots and their corresponding S_q for three different temperatures, indicated as vertical lines in the plots from the top panel. At the lowest simulated temperature, a spiral phase is stabilized, but an intermediate bimeron phase is clearly seen at higher T.

a ferromagnetic phase at low temperature with an intermediate skyrmion gas phase. In the higher-temperature snapshot, which corresponds to the highest value of the chirality, we can also see that although the system has a net chirality, thermal fluctuations break the skyrmion and less-defined chiral structures are seen.
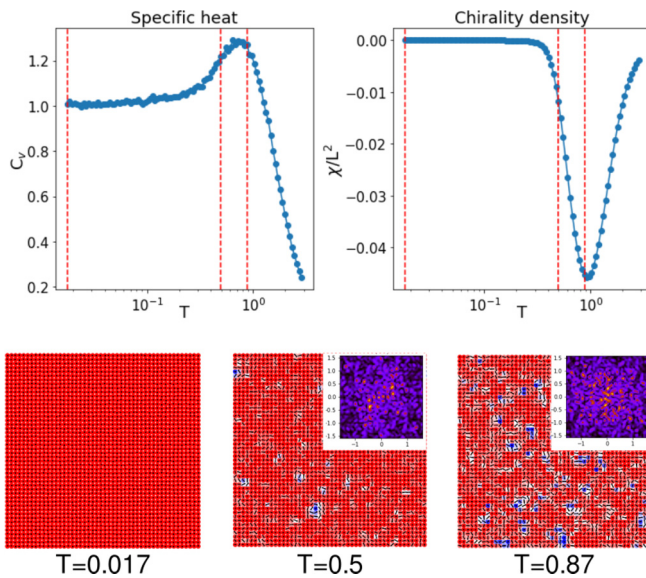

FIG. 3. Monte Carlo simulations for $D = 1$, $B = 0.9$. (top) specific heat, magnetization, and chirality as a function of temperature. (bottom) three snapshots and their corresponding S_q for three different temperatures, indicated as vertical lines in the plots from the top panel. At the lowest simulated temperature, the system is in the ferromagnetic phase, but an intermediate skyrmion gas phase is clearly seen at higher T.

Following the discussion above, the identification of the intermediate phases and the construction of a complete detailed B-T phase diagram requires a combination of resources, including calculation of the scalar chirality, inspection of the structure factor, and inspection of the real-space configurations. In this work, our goal is to use machine learning techniques to assist in the detection of the intermediate "nonstandard" phases and in the construction of this phase diagram, avoiding a snapshot-by-snapshot inspection. In the next section we describe our machine learning approach and present our results using a convolutional neural network.

III. MACHINE LEARNING APPROACH

Here we describe how we are going to use machine learning techniques to construct a complete B-T phase diagram. We present the steps in Fig. 4.

First, in order to train and validate the ML algorithms we produce snapshots for the five different low-temperature phases (Bm, Fm, SkG, SkX, Sp) using Monte Carlo simulations. We use the model Hamiltonian presented in Eq. (1), but we only take three values of the DM interaction, $D = 0.5, 1.0, 1.5$, for training and validation. Since we are taking low-temperature configurations, from Fig. 1 it can be clearly seen that the dataset will be very unbalanced, since the intermediate Bm and SkG phases are only stable in a very narrow range of magnetic field. Therefore, we run more simulations in these magnetic field ranges, in order to increase the number of Bm and SkG snapshots. The Monte Carlo simulations are done with the Metropolis algorithm combined with overrelaxation for a 48×48 square lattice, taking 10^5 MC steps for thermalization and twice as many to take measurements. Each simulation is done by fixing a value of B and using the annealing technique to take the system from $T = 3$ to $T = 0.017$. For each parameter set, ≈ 30 copies with independent seeds were done.

Second, we train a convolutional neural network (CNN) for classification using the low-T dataset, where we have labeled the snapshots (this is an instance of *supervised learning*). As in previous works [16], we only use as input the projection of the spins along the magnetic field S^z. This has the clear advantage of reducing the dataset by a factor of three. Nonetheless, inclusion of the in-plane components of the spins would be needed to distinguish between Bloch and Néel skyrmions and also antiskyrmions, which is not the case in this work. We do not use any other variable (D, B, specific heat, chirality, etc.), to make sure that resulting model does not depend on parameters, but only on the configurations, and it can thus be potentially used for snapshots resulting from different Hamiltonians. Since we aim to construct a B-T phase diagram, we also take snapshots at the highest temperatures, i.e., in the paramagnetic phase (Pm), at high ($B = 0.9$) and zero magnetic field, where the system will not stabilize at low temperatures in a SkX phase. We later discuss the effect of including these snapshots.

Third, we apply the trained network to a test set, which we construct with low-T snapshots obtained for other values of the DM interaction, $D = 0.75, 1.25$, not used in training. The value of D controls the size of the skyrmions and the spirals. Therefore, our idea here is to see whether the network can correctly identify topological structures in a parameter
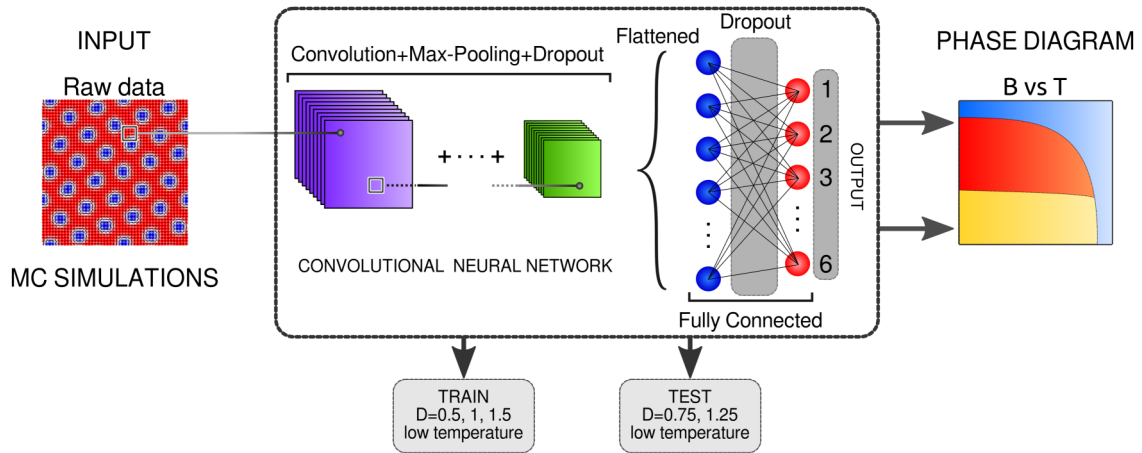
FIG. 4. Steps from the machine learning approach used in this work. The dataset consists of S^z components from spin configurations obtained from Monte Carlo simulations. A convolutional neural network classification model was constructed, using the lowest-temperature configurations at three values of the DM coupling ($D = 0.5, 1, 1.5$) and a subset of high-temperature data for training and validation, separating in six different phases: spirals, bimerons, skyrmion crystal, skyrmion gas, ferromagnetic, and paramagnetic. A set of lowest temperature samples for different DM values ($D = 0.75, 1.25$) was used for testing. The resulting CNN classification model was applied for configurations in a wide range of temperature and magnetic field, to construct a complete (B, T) phase diagram. Details of the CNN architecture are shown in the Appendix.

region where it has not been trained. This would be extremely useful, since it would mean that it is only necessary to train a technique in a small region of parameter space, and then it may be applied to any other values.

Finally, to construct the complete B-T phase diagram, we apply the trained CNN to classify snapshots for all temperatures and magnetic fields. We do this for different values of D, and we compare the resulting phase diagrams with the chirality density phase diagram obtained from MC simulations.

Below, we present a table detailing the dataset used in this work.

A. Convolutional neural network results

Convolutional neural networks (CNNs) have been used with great success in pattern and image recognition [39]. Details of the architecture of the CNN used in this work are given in the Appendix. The training dataset was split in 80% for training and 20% for validation, and the S^z spin component was rescaled from $[-1, 1]$ to $[0,1]$. The output of the CNN is a probability for each class (or phase), and we define the class of a given snapshot as the one that has the highest probability.

As a first step, we apply the CNN to the $D = 0.5, 1.0, 1.5$ dataset, including all five low temperature phases and the paramagnetic phase. We obtain an accuracy of 99.9% in the training set, and 97.5% in the validation set. Then, we use this trained CNN to predict the phases for our test set, $D = 0.75, 1.25$, and obtain a slightly lower, but still satisfactory, accuracy of 91%. To analyze if there are specific phases where the CNN is misclassifying the snapshots, we calculate the confusion matrices (CM) for the training, validation and test set, which are to be read as follows: the ith row indicates the true label for the ith class, and the jth row, the predicted label for the jth class. Therefore, at a quick glance, if the off-diagonal elements of the CM matrices are significantly lower than the diagonal ones, it would mean that there are

few misclassified snapshots in that dataset. We present the confusion matrices for the three sets below, where the classes (phases) are ordered alphabetically (Bm, Fm, Pm, SkG, SkX, Sp):

$$CM_{\text{train}} = \begin{pmatrix} 163 & 0 & 0 & 0 & 0 & 7 \\ 0 & 262 & 0 & 0 & 0 & 0 \\ 0 & 0 & 473 & 0 & 0 & 0 \\ 0 & 5 & 0 & 187 & 0 & 0 \\ 6 & 0 & 0 & 0 & 214 & 0 \\ 0 & 0 & 0 & 0 & 0 & 281 \end{pmatrix}, \quad (2)$$

$$CM_{\text{val}} = \begin{pmatrix} 36 & 0 & 0 & 0 & 1 & 1 \\ 0 & 68 & 0 & 0 & 0 & 0 \\ 0 & 0 & 127 & 0 & 0 & 0 \\ 0 & 1 & 0 & 47 & 0 & 0 \\ 1 & 0 & 0 & 0 & 39 & 0 \\ 0 & 0 & 0 & 0 & 0 & 79 \end{pmatrix}, \quad (3)$$

$$CM_{\text{test}} = \begin{pmatrix} 101 & 0 & 0 & 0 & 11 & 22 \\ 0 & 10 & 0 & 0 & 0 & 0 \\ 0 & 0 & 60 & 0 & 0 & 0 \\ 0 & 3 & 0 & 87 & 0 & 0 \\ 11 & 0 & 0 & 30 & 267 & 0 \\ 9 & 0 & 0 & 0 & 0 & 351 \end{pmatrix}. \quad (4)$$

Inspecting the CMs, we can see that, not surprisingly, the CNN has more trouble classifying the intermediate phases, Bm and SkG (first and fourth rows). Notice that the test dataset contains less ferromagnetic and paramagnetic phases (Table I), where the network has more accuracy: from the CMs, reading rows two and three, it can be seen that all Fm and Pm snapshots where correctly classified. To further analyze the misclassified data, we first present as an example a misclassified snapshot from the test set in Fig. 5, left. This is a Bm phase, where there are some bimerons among skyrmions arranged in a lattice. If we look at the probabilities calculated for this configuration by the CNN, we see that it assigns it as

TABLE I. Data set. Snapshots at $D = 0.5, 1.0, 1.5$ were used for training and validation, and $D = 0.75, 1.25$ were used as the test set. Bm: bimerons, Fm: ferromagnetic, Pm: paramagnetic, SkG: skyrmion gas, SkX: skyrmion crystal, Sp: spiral.

Phases or classes	$D = 0.5, 1.0, 1.5$	$D = 0.75, 1.25$
Bm	208	134
Fm	330	10
Pm	600	60
SkG	240	90
SkX	260	308
Sp	360	360
Total	1998	962

a SkX with a probability of 55%, but the Bm class, which is the correct class, has the second highest probability of 44%. Then, there is not a large difference between the two highest probabilities assigned by the CNN, i.e., the highest probability assigned is not significantly high. We then plot in Fig. 5, left, a histogram of the highest probability assigned to the chosen phase to the whole test set and compare it with the same histogram obtained only for misclassified snapshots. We can clearly see that in the misclassified subset the CNN assigns much lower probabilities than to the correctly classified ones, since the peak for the probabilities higher than 0.9 is not seen in the histogram of the misclassified data. Comparing the counts from the histogram, it may also be seen that there are significantly less misclassified snapshots, suggesting a high accuracy.

To further explore the network, to see how to get the low-temperature phases in the test dataset, we plot the probability of all six phases as a function of magnetic field, calculated for all low temperature configurations in the test dataset, $D = 1.25$ and $D = 0.75$, at the top row of Fig. 6. The bottom row shows the low-temperature chirality as a function of magnetic field, calculated as the mean value and standard deviation over 30 independent realizations per field of the thermal

FIG. 6. (top) Probabilities calculated by the trained CNN as a function of B for the test set values of the DM interaction, $D = 1.25$ (left) and $D = 0.75$ (right). (bottom) Chirality density obtained from MC simulations as a function of magnetic field, averaged over 30 independent copies. Error bars indicate the standard deviation.

average obtained from MC simulations. In the $D = 1.25$ case, for the chosen range of B, it can clearly be seen that the CNN identifies the low-B configurations as spirals, and the higher-B snapshots as skyrmion crystal. At a certain point of B, the probability for the bimeron phase raises significantly, indicating a small Bm phase at low T. Inspection of the chirality agrees with this picture: it is zero at low fields, and it has a finite and constant value at higher B. Between these values, intermediate points can be identified, matching the Bm prediction. For $D = 0.75$, more phases can be seen in a smaller range of magnetic field. We may also identify intermediate regions, so that the selected phases as a function of the magnetic field are spiral, bimeron, skyrmion crystal, skyrmion gas, and paramagnetic. No high probability can be seen for the paramagnetic phase for either value of D, which is consistent with the fact that we are inspecting low-temperature configurations.

We now proceed to construct the complete B-T phase diagram, applying the trained CNN to snapshots for all temperatures and magnetic fields. In Fig. 7 we plot the resulting phase diagrams for $D = 1.0$, where only the lowest T and the $B = 0$ and $B = 0.9$ high-T configurations where used for training and validation, and for $D = 0.75$, which was not used to train the CNN. To compare the results, we plot the chirality density obtained from Monte Carlo simulations. We can see that there is a very good agreement between both phase diagrams and the χ density. Moreover, we can see that there is no "phase mixing:" the CNN does not assign for example a spiral at high magnetic field, or an ordered phase at high temperature.

Although the CNN seems to overestimate slightly some intermediate regions, for example the SkG phase at high fields
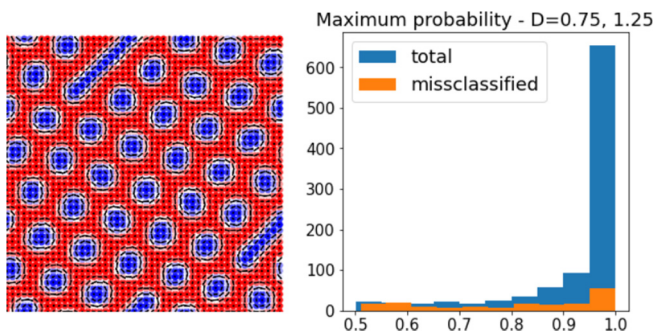

FIG. 5. (left) Example of a misclassified snapshot for the test dataset. The CNN assigns a 55% probability to the SkX phase, and 44% to the Bm phase. (right) Histograms of the maximum probability for the complete test set (blue) and for the misclassified configurations in the test set (orange). It can be seen that there is a larger portion of misclassified snapshots with lower highest probabilities, and that the highest probabilities correspond to correctly classified configurations.
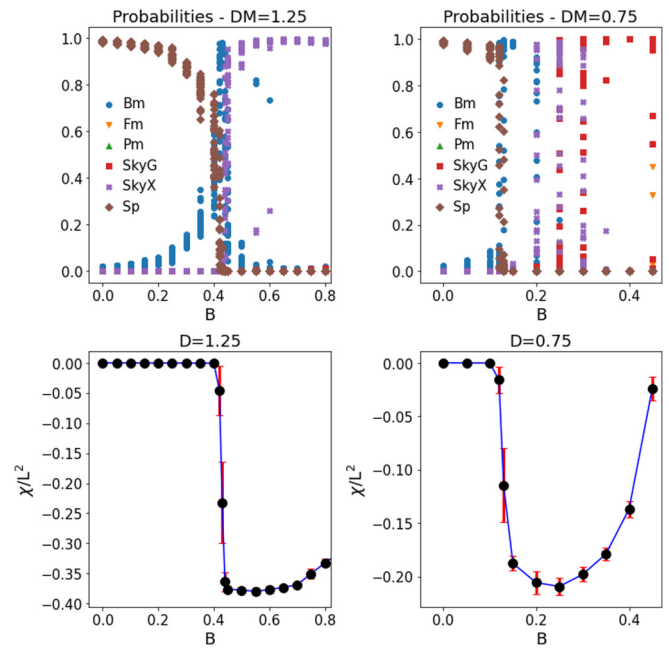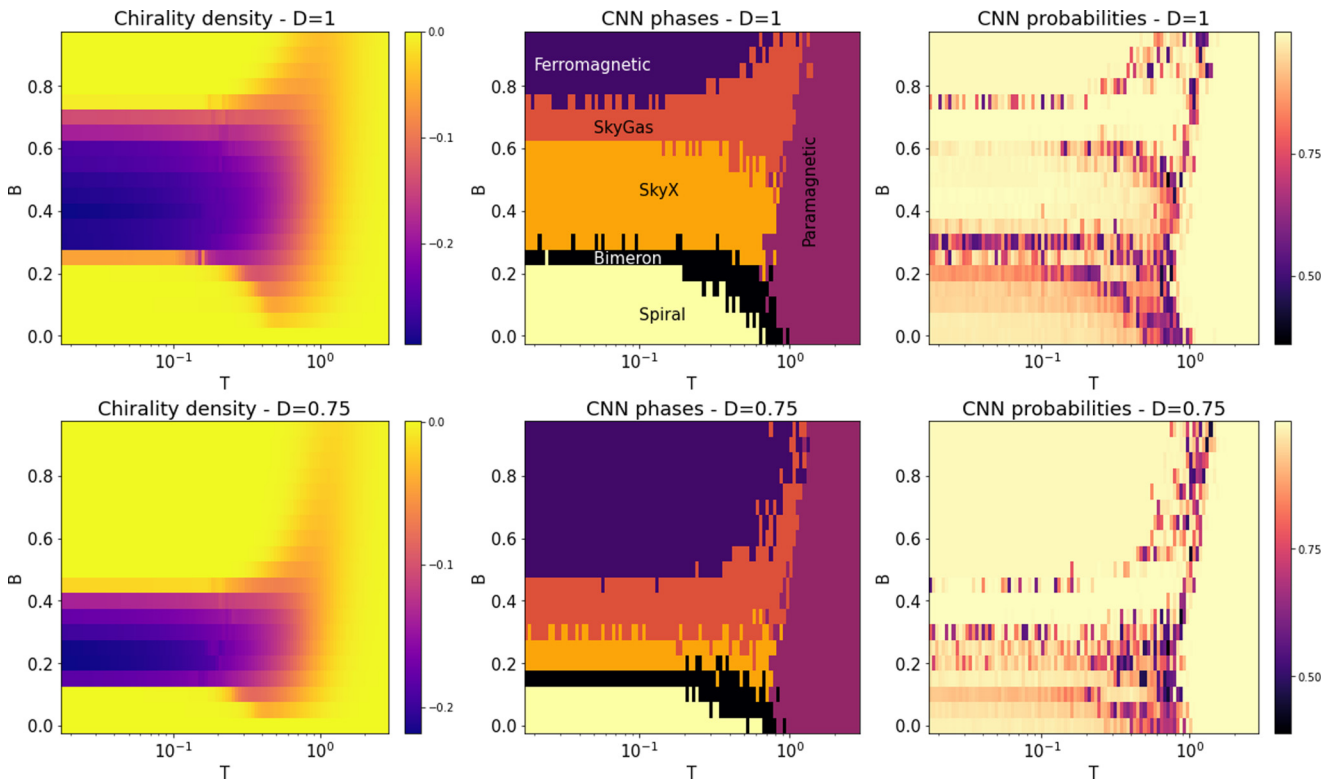
FIG. 7. Phase diagrams for $D = 1$ (top) and $D = 0.75$ (bottom). First column shows the chirality density obtained from MC simulations. Middle column shows the phases predicted by the CNN. Right column shows the probabilities for the phases predicted by the CNN.

or the Bm phase at very low fields, it can also correctly identify what may be considered "tricky" configurations, such as single skyrmions in a ferromagnetic background. We plot in Fig. 8 three snapshots at high field that the CNN labels as SkG: one is a single well-formed skyrmion at low T (left), and the other two are at higher temperatures: in one case, skyrmion-like structures may still be identified (center), in the other case, thermal fluctuations have destroyed the characteristic skyrmion like structures.

To continue analyzing the output of the CNN, in the right column of Fig. 7 we plot the phase diagram of the maximum probability assigned to the chosen class. It can be seen that the CNN classifies with high probability in the middle of the different phases, but it gets lower in the interphases, both with magnetic field and temperature. In this sense, the probability
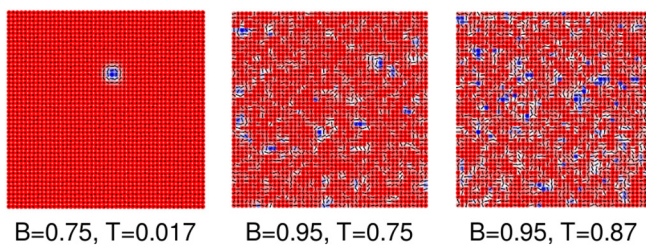

FIG. 8. Examples of snapshots classified as skyrmion gas, $D = 1$ (left) One single skyrmion at the lowest temperature, $T = 0.017$, for $B = 0.75$. (center) Skyrmion gas intermediate phase induced by temperature for $T = 0.75$, $B = 0.95$. (right) Snapshot of the configuration at $T = 1.0$, $B = 0.95$.

gives us valuable physical information, specially in regions with stronger thermal fluctuations.

We may then wonder two things: whether it is necessary to include a paramagnetic phase, and what would change if we only classified with the three well-defined phases (Fm, SkX, Sp). As was stated in previous works [16,19], fluctuations in the probability may gives us an insight on whether to expect intermediate or different phases. We thus proceed as we did before for the six-phase dataset, constructing three different subsets: five low-T phases (Bm, Fm, SkG, SkX, Sp), three low-T phases and the paramagnetic one (Fm, Pm, SkX, Sp), and only three low-T phases (Fm, SkX, Sp). For each case, a different CNN model was trained, but we maintained the architecture of the network. As a comment, excluding the intermediate Bp and SkG phases enhances the accuracy: for the last two data subsets the accuracy is 100% for the training, validation and test sets. We plot the phase diagrams and the corresponding probabilities for $D = 1$ in Fig. 9.

First, we see that including the paramagnetic phase in the dataset is helpful to define the temperature limits of the low-T configurations. In the case where we included intermediate phases but excluded the paramagnetic class (Bm, Fm, SkG, SkX, Sp) Fig. 9, top, we see that, at low magnetic fields, the assigned probabilities drop at higher temperature, suggesting that the classification does not work there (and thus, that a different phase may have to be considered), although this may not said looking at higher magnetic fields. Then, if we only take the three phases that would be stable in the $T \rightarrow 0$ limit (spirals, skyrmions crystals and ferromagnetic), we see that the inclusion of the paramagnetic phase (Fm, Pm, SkG, SkX, Sp) does not only help to establish the temperature limits
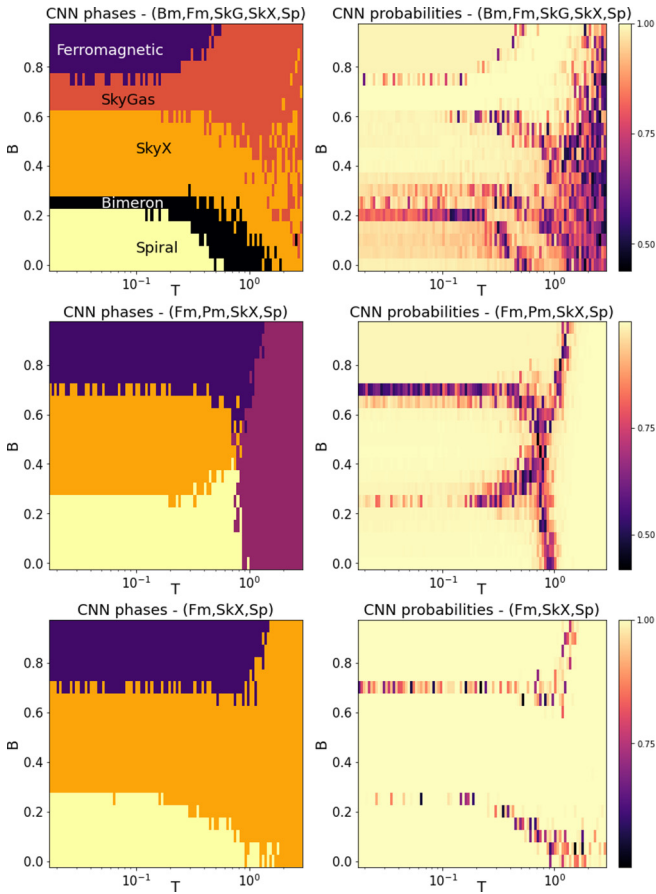
FIG. 9. Phase diagrams (left) and probabilities (right) assigned to each phase obtained with the trained CNN for $D = 1$ and three different subsets of the data set: five phases without the paramagnetic case (Bm, Fm, SkG, SkX, Sp), three phases with the paramagnetic phase—no intermediate phases (Fm, SkX, Sp, Pm), three phases without intermediate or paramagnetic cases (Fm, SkX, Sp).

of these low-T phases, but it also favors the definition of possible intermediate phases, given by the areas where the probabilities are lower, both with temperature and magnetic field (Fig. 9, middle panel). This is clearly in contrast with taking only the three low-T phases (Fm, SkX, Sp), bottom panel of Fig. 9. In that case, the probabilities drop in a narrow region in magnetic field, and clearly do not drop at higher temperatures, showing that the CNN underestimates the intermediate phases, especially the bimerons at low magnetic fields. Nonetheless, this comparison allows us to propose that training a CNN with well-defined phases, such as (Fm, Pm, SkX, Sp), and applying it to a whole range of temperature and magnetic field to unknown configurations also serves as a tool to identify regions where there might be possible new phases.

B. Comparison with other classification methods

In this section, we resort to other less complex ML classification techniques, to compare with the CNN. First, we choose the support vector machine (SVM) [39,40]. Using the Scikit Learn package, we proceed as before, with the six class dataset (Bm, Fm, Pm, SkG, SkX, Sp). We use cross validation to optimize the regularization parameter "C" and the kernel
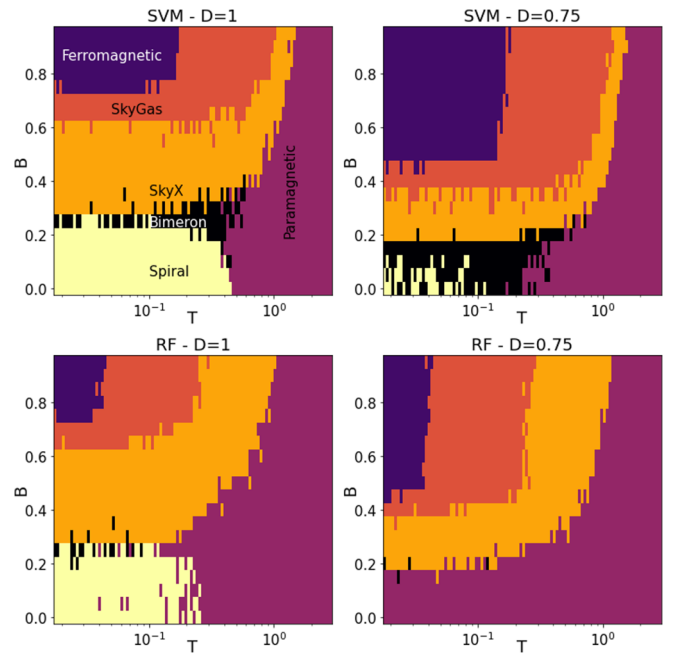

FIG. 10. Phase diagrams obtained with SVM (top) and rf (bottom), for $D = 1$ (left column) and $D = 0.75$ (right column).

coefficient "gamma," choosing a radial basis function as kernel. The resulting SVM has a 99.9% accuracy in the training set, and 95% in the validation set. However, the accuracy drops when applying it to the test set, where it goes to 78%. Inspection of the CM shows that the most notable problem lies in the spiral class: more than half of the spiral configurations are classified as paramagnetic. Given that the test set is formed by other values of D not used in training, we may say that the SVM does not generalize as well as the CNN. We compare the complete B-T phase diagrams for $D = 1$ and $D = 0.75$ in Fig. 10, top row, where we confirm this last statement. For $D = 1$, which was used for training, the phase diagram is schematically correct at low temperatures. As the temperature increases, it is still consistent with the known phase diagram at low fields, but fails at higher fields, especially where there is an intermediate SkX high T and high B phase. This is even worse for $D = 0.75$, where the classification is problematic even at low temperature. Then, the SVM may be a good tool to explore a first version of a phase diagram, provided that D (basically, skyrmion and spiral size) is fixed.

Second, we train a random forest (RF) [39,40], which is a collection of decision tree (DT) classifiers. As before, using cross validation we optimized the number of DTs and the maximum depth of each DT. As with the SVM case, the accuracy in the training set is high, 100%, but drops to 89% in the validation set. It gets worse when changing the size of the textures: the accuracy is 43% in the test set, showing that the RF is not a good tool to extend the classification to other configurations. We illustrate this by constructing the phase diagrams, shown in the bottom row of Fig. 10. For $D = 1$, we see that the RF reproduces the behavior at low T, consistent with the accuracy score in the training set, but it does not generalize well when applying it to higher-temperature configurations. Clearly, inspecting the $D = 0.75$ case, we see

that the RF practically does not detect intermediate phases and fails dramatically at low magnetic fields, where it assigns a paramagnetic phase at low temperature. This further supports the claim that this technique does not generalize well to values of D that have not been used in training.

IV. CONCLUSIONS

Our main goal in this work was to present a machine learning approach to classify different types of topological phases, including skyrmions and bimerons, to construct a complete detailed phase diagram, and that it would be able to generalize to different skyrmion sizes. To this end, we chose a convolutional neural network and we constructed the dataset from Monte Carlo simulations, enhanced for intermediate phases (bimerons and skyrmion gas). We trained and validated the CNN using only the lowest-temperature snapshots, excluding other measurements or parameters from the Hamiltonian used to generate this configurations. In this way, our resulting trained CNN would be applicable to other configurations or images, provided they are formatted as the input data. The training and validation sets where chosen for fixed values of the DM interaction, i.e., three characteristic skyrmion and spiral sizes. To test whether the CNN can generalize to other skyrmion sizes, we chose as the test set two different DM values. Since we are interested in building a complete phase diagram, we included high-temperature snapshots in the paramagnetic phase.

The resulting CNN model was then applied to configurations for a wide range of temperature and magnetic field, for different values of D, to construct the complete and detailed $B\text{-}T$ phase diagram. Comparing with the chirality density obtained from Monte Carlo simulations, we find a remarkable agreement, even in the intermediate phases. This shows that CNNs are a powerful tool not only to construct a complete phase diagram but also to extend this type of work to other models. Given that the only input for the CNN is the spin configuration, the resulting trained CNN models are applicable to snapshots obtained with simulations for other Hamiltonians, or even real-space experimental images.

We also discuss the importance of including paramagnetic and intermediate phases, constructing the phase diagram for different subsets of the data. We see that, as a first approach, taking only the three well-ordered low-temperature phases may help to determine possible intermediate phases, although this fails at higher temperature unless the paramagnetic phase is included.

Finally, we used the same approach choosing two other machine learning classification techniques: support vector machine and random forest. In both cases, there is a very high accuracy in the training set, but it drops significantly when applying the resulting algorithm to snapshots with different skyrmion and spiral sizes, specially in the RF case. This shows that these techniques, very powerful for other tasks, do not generalize as well as the CNNs.

We hope this work contributes to the ongoing work resorting to machine learning techniques in condensed matter. In the future, we expect to continue this type of work in other nontrivial topological phases such as antiferromagnetic skyrmions [32,41–43], antiskyrmions [44,45], chiral phases [46,47], and spin liquids [48–50].

APPENDIX

Here we describe in detail the architecture of the CNN network, which we maintained when analyzing all the subsets of data, with the exception of the last layer, where the number of units matches the number of classes (phases).

The CNN was constructed with four convolutional layers with 32 filters of size three, no padding, and the activation function ReLu. Each of these layers was followed by a Max Pooling layer of pool size two and a Dropout layer with dropout value of 0.25. Then, the system was flattened and followed by a Dense layer of 128 nodes and activation function ReLu, a Dropout layer with dropout 0.25, and finally a Dense output layer with activation function softmax.

We chose cross entropy as the error, scalar gradient descent as the optimizer, and a learning rate 0.05. The CNN was trained in 200 epochs, with batch size 32. The CNN was implemented in TensorFlow [51].

[1] G. Carleo and M. Troyer, Science **355**, 602 (2017).

[2] B. S. Rem, N. Käming, M. Tarnowski, L. Asteria, N. Fläschner, C. Becker, K. Sengstock, and C. Weitenberg, Nat. Phys. **15**, 917 (2019).

[3] L. Wang, Phys. Rev. B **94**, 195105 (2016).

[4] E. P. van Nieuwenburg, Y.-H. Liu, and S. D. Huber, Nat. Phys. **13**, 435 (2017).

[5] J. Carrasquilla and R. G. Melko, Nat. Phys. **13**, 431 (2017).

[6] A. M. Samarakoon, K. Barros, Y. W. Li, M. Eisenbach, Q. Zhang, F. Ye, V. Sharma, Z. L. Dun, H. Zhou, S. A. Grigera, C. D. Batista, and D. A. Tennant, Nat. Commun. **11**, 892 (2020).

[7] A. M. Samarakoon, D. Alan Tennant, Feng Ye, Qiang Zhang, and S. A. Grigera, arXiv:2110.15817.

[8] J. Greitemann, K. Liu, L. D. C. Jaubert, H. Yan, N. Shannon, and L. Pollet, Phys. Rev. B **100**, 174408 (2019).

[9] J. Greitemann, K. Liu, and L. Pollet, J. Phys.: Condens. Matter **33**, 054002 (2021).

[10] K. Liu, N. Sadoune, N. Rao, J. Greitemann, and L. Pollet, Phys. Rev. Research **3**, 023016 (2021).

[11] N. Rao, K. Liu, M. Machaczek, and L. Pollet, Phys. Rev. Research **3**, 033223 (2021).

[12] N. Rao, K. Liu, and L. Pollet, Phys. Rev. E **104**, 015311 (2021).

[13] A. Fert, N. Reyren, and V. Cros, Nat. Rev. Mater. **2**, 17031 (2017).

[14] B. Göbel, I. Mertig and O. A. Tretiakovc, Phys. Rep. **895**, 1 (2021).

[15] V. Bonbien, F. Zhuo, A. Salimath, O. Ly, A. Abbout, and A. Manchon, J. Phys. D **55**, 10 (2021).

[16] I. A. Iakovlev, O. M. Sotnikov, and V. V. Mazurenko, Phys. Rev. B **98**, 174411 (2018).

[17] J. S. Salcedo-Gallo, C. C. Galindo-González, E. Restrepo-Parra, J. Magn. Magn. Mater. **501**, 166482 (2020).

[18] A. Y. Deviatov, I. A. Iakovlev, and V. V. Mazurenko, Phys. Rev. Appl. **12**, 054026 (2019).

[19] V. K. Singh and J. H. Han, Phys. Rev. B **99**, 174426 (2019).

[20] T. Matthies, A. F. Schäffer, T. Posske, R. Wiesendanger, and E. Y. Vedmedenko, Phys. Rev. Appl. **17**, 054022 (2022).

[21] M. Kawaguchi, K. Tanabe, K. Yamada, T. Sawa, S. Hasegawa, M. Hayashi, and Y. Nakatani, npj Comput. Mater. **7**, 20 (2021).

[22] W. Wang, Z. Wang, Y. Zhang, B. Sun, and K. Xia, Phys. Rev. Appl. **16**, 014005 (2021).

[23] M. Ezawa, Phys. Rev. B **83**, 100408(R) (2011).

[24] R. L. Silva, L. D. Secchin, W. A. Moura-Melo, A. R. Pereira, and R. L. Stamps, Phys. Rev. B **89**, 054434 (2014).

[25] A. O. Leonov, C. Pappas, and I. I. Smalyukh, Phys. Rev. B **104**, 064432 (2021).

[26] B. Göbel, A. Mook, J. Henk, I. Mertig, and O. A. Tretiakov, Phys. Rev. B **99**, 060407(R) (2019).

[27] X. Z. Yu, Y. Onose, N. Kanazawa, J. H. Park, J. H. Han, Y. Matsui, N. Nagaosa, and Y. Tokura, Nature (London) **465**, 901 (2010).

[28] K. von Bergmann, A. Kubetzka, O. Pietzsch, and R. Wiesendanger, J. Phys.: Condens. Matter **26**, 39 (2014).

[29] M. Hirschberger, T. Nakajima, S. Gao, L. Peng, A. Kikkawa, T. Kurumaji, M. Kriener, Y. Yamasaki, H. Sagayama, H. Nakao, K. Ohishi, K. Kakurai, Y. Taguchi, X. Yu, T.-h. Arima, and Y. Tokura, Nat. Commun. **10**, 5831 (2019).

[30] Y. Yasui, C. J. Butler, N. D. Khanh, S. Hayami, T. Nomoto, T. Hanaguri, Y. Motome, R. Arita, T.-h. Arima, Y. Tokura and S. Seki, Nat. Commun. **11**, 5925 (2020).

[31] S. Mühlbauer, B. Binz, F. Jonietz, C. Pfleiderer, A. Rosch, A. Neubauer, R. Georgii, and P. Böni, Science **323**, 5916 (2009).

[32] H. D. Rosales, D. C. Cabra, and P. Pujol, Phys. Rev. B **92**, 214439 (2015).

[33] W. Legrand, D. Maccariello, F. Ajejas, S. Collin, A. Vecchiola, K. Bouzehouane, N. Reyren, V. Cros, and A. Fert, Nat. Mater. **19**, 34 (2020).

[34] H. Jani, J.-C. Lin, J. Chen, J. Harrison, F. Maccherozzi, J. Schad, S. Prakash, C.-B. Eom, A. Ariando, T. Venkatesan, and P. G. Radaelli, Nature (London) **590**, 74 (2021).

[35] S. Gao, H. D. Rosales, F. A. Gómez Albarracín, V. Tsurkan, G. Kaur, T. Fennell, P. Steffens, M. Boehm, P. Čermák, A. Schneidewind, E. Ressouche, D. C. Cabra, C. Rüegg, and O. Zaharko, Nature (London) **586**, 37 (2020).

[36] X. Yu, J. Magn. Magn. Mater. **539**, 168332 (2021).

[37] A. Bogdanov and A. Hubert, J. Magn. Magn. Mater. **138**, 255 (1994).

[38] I. A. Iakovlev, O. M. Sotnikov, and V. V. Mazurenko, Phys. Rev. B **97**, 184415 (2018).

[39] A. Géron, *Hands-On Machine Learning with Scikit-Learn, Keras, and TensorFlow* (O'Reilly, Canada, 2019).

[40] R. Bishop, *Pattern Recognition and Machine Learning* (Springer, Singapore, 2006).

[41] M. E. Villalba, F. A. Gómez Albarracín, H. D. Rosales, D. C. Cabra, Phys. Rev. B **100**, 245106 (2019).

[42] M. Mohylna and M. Zukovic, J. Magn. Magn. Mater. **527**, 167755 (2021).

[43] M. Mohylna and M. Zukovic, J. Magn. Magn. Mater. **546**, 168840 (2022).

[44] D. S. Kathyat, A. Mukherjee, and S. Kumar, Phys. Rev. B **104**, 184434 (2021).

[45] A. Mukherjee, D. S. Kathyat, and S. Kumar, Phys. Rev. B **105**, 075102 (2022).

[46] K. Essafi, O. Benton, and L. D. C. Jaubert, Phys. Rev. B **96**, 205126 (2017).

[47] F. A. Gómez Albarracín and P. Pujol, Phys. Rev. B **97**, 104419 (2018).

[48] L. Balents, Nature (London) **464**, 199 (2010).

[49] F. A. Gómez Albarracín and H. D. Rosales, Phys. Rev. B **93**, 144413 (2016).

[50] K. Essafi, O. Benton, and L. D. C. Jaubert, Nat. Commun. **7**, 10297 (2016).

[51] M. Abadi *et al.* (2015), software available from tensorflow.org